Modeling and Simulation of the Solar Collector Using Different Approaches

Kazimierz Kamiński and Tomasz Krzyżyński

Abstract This paper presents numerical and experimental investigation of a flat-plate solar collector. Fluid flow and heat transfer in the collector panel are studied by means of distributed-character modeling method (D-C) and computational fluid dynamics (CFD) calculations. Further, experimental investigations of the solar collector panel are carried out. The solar collector thermal efficiency is determined according to EN ISO 9806:2013 standard and the absorber temperature distribution is measured through the back side of collector panel. The measured collector thermal efficiency and absorber temperature distribution are compared with the results from two different numerical models. The paper is summarized by discussion about utility value of tested numerical models in various research areas.

Nomenclature

A	Area (m^2)
c	Heat capacity (J kg^{-1} K^{-1})
d	Inner diameter (m)
D	Outer diameter (m)
G_{sun}	Solar radiation (W m^{-2})
g	Thickness (m)
V	Volume (m^3)
W	Width (m)
L	Length (m)
Q	Power output (W)
v	Velocity (m s^{-1})
T	Temperature (°C)
q	Heat flux (W)

K. Kamiński (✉) · T. Krzyżyński
Faculty of Technology and Education, Koszalin University of Technology, Koszalin, Poland
e-mail: kazimierz.kaminski@tu.koszalin.pl

T. Krzyżyński
e-mail: tomasz.krzyzynski@tu.koszalin.pl

J. Awrejcewicz et al. (eds.), *Mechatronics: Ideas, Challenges, Solutions and Applications*, Advances in Intelligent Systems and Computing 414,
DOI 10.1007/978-3-319-26886-6_9

α	Heat transfer coefficient (W m^{-2} K^{-1})
λ	Thermal conductivity (Wm^{-1} K^{-1})
$(\tau\alpha)$	Transmittance–absorbtance product
$\dot{m}$	Mass flow rate (kg s^{-1})
σ	Stefan-Boltzman constant (W m^{-2} K^{-4})
S	Surface area (m^2)
ρ	Density (kg m^{-3})
ε	Emissivity
η	Efficiency
η_0	Optical efficiency
a_1	Heat loss coefficient (W m^{-2} K^{-1})
a_2	Temperature dependence of a_1 (W m^{-2} K^{-2})
$T * m$	Reduced temperature difference (m^2 K W^{-1})
Nu	Nusselt number
Re	Reynolds number
Pr	Prandtl number
Γ	Diffusive coefficient

Subscripts

a	Absorber
p	Pipe
f	Fluid
m	Middle
in	Inlet
out	Outlet
amb	Ambient

1 Introduction

A flat-plate solar collector is a low-cost and the easiest-to-fabricate device which can effectively transform solar energy into useful heat. For the same reason, solar collectors are often used in domestic water heating systems, agriculture drying applications, and industrial heat processing. Figure 1 shows a typical, commonly used flat-plate solar collector.

The energy conversion, which occurs inside solar collector, is carried out by a flat-plate, high conductive metal sheet called as the absorber plate. Useful heat, collected in the absorber plate, is taken away by working fluid, pumped through the flow channels which are welded to the absorber plate. This type of absorbers is called fin-and-tube and can be made in two basic configurations. The first one is a serpentine-tube absorber, where flow is driven through only one, specially formed

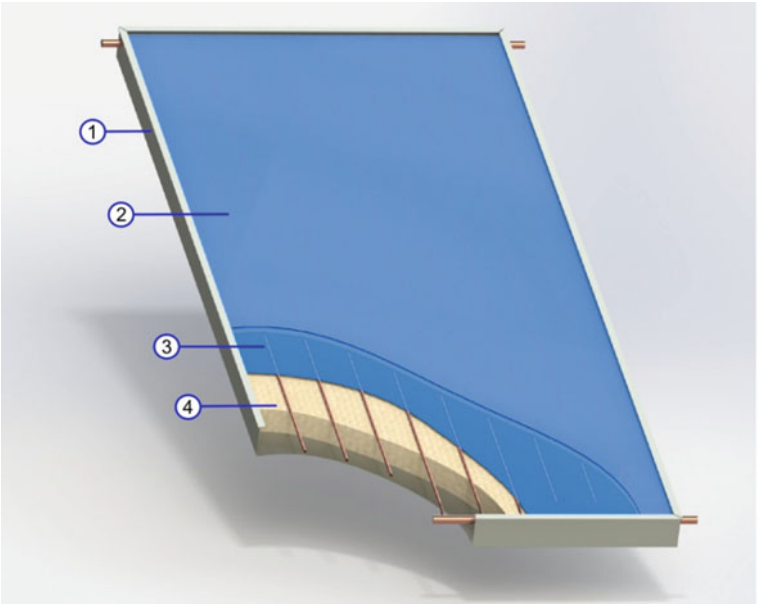

Fig. 1 Solar flat-plate collector: *1* collector housing; *2* glass cover; *3* absorber; *4* thermal insulation

flow channel. Because of quite a complicated fabrication process this type of solar collector is often priced similarly to evacuated heat pipe solar collectors. The second type, more widespread and cheaper, is parallel tube solar collector. In this type of collector, flow of working fluid is driven through a number of straight flow channels, mounted to inlet and outlet manifolds. Figure 2 shows basic flow channels configurations applied in commonly used solar flat-plate collector.

In most cases, solar flat-plate collectors are simple devices which consist of thermal isolated assembly of flat metal sheet connected to flow pipes. During the last few decades, this simple design has been well optimized and improved. However, there is still an interest in more effective solutions and design

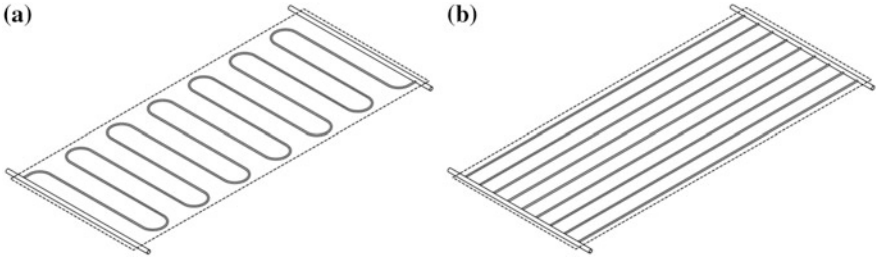

Fig. 2 Basic configuration of solar collector absorber flow channels configurations: **a** serpentine-tube (meander); **b** parallel tube (harp)

optimizations. This improvement process needs to be carried out with appropriate numerical models and experiments.

In order to estimate the thermal performance of the solar collector, which is operated in specific climate conditions, many different models presented in literature can be used. The differences between those approaches basically depend on complexity and established assumptions and simplifications. It is important to know which one can be used to achieve the required calculation goal.

2 Solar Flat-Plate Collector Modeling

In general, it is quite difficult to numerically obtain comprehensive information about heat exchange process and thermal behavior of a solar collector. This is mainly because of the complexity of this problem and high number of parameters affecting it. In spite of these difficulties, several useful numerical approaches have been developed. A part of these methods are based on the well-known Hottel-Whillier-Bliss theory [1], which is suitable for almost every kind of solar collectors. These methods provide quite simple form of differential equations, with distributed character (D-C), which can be solved with the finite differences method. Another group of solar collector modeling approaches, highly developed during the last years, are CFD numerical methods [2].

In order to compare the results from these two types of modeling approaches, the simplified distributed-character model was built and CFD modeling procedure using *Ansys Fluent 13* was carried out.

2.1 Distributed-Character Model

The solar collector thermal efficiency is strongly correlated with the internal temperature distribution. In order to form highly accurate numerical model with proper heat losses, the spatial absorber temperature needs to be obtained. Since the single-capacitance models are not able to predict the inside collector temperature distribution, the distributed-character modeling method was used.

The proposed distributed-character model is suitable for almost every kind of solar collector design. It allows obtaining a lot of useful information about modeled heat exchanging process. The elaborated model consists of M nodes perpendicular to the flow direction (e.g., absorber discrete elements, flow channels, and working fluid) and N nodes in flow direction. As a result, the $N \times M$ system of ordinary differential equations is obtained and solved with the finite difference method. Similar forms of models were presented by Kimminga [3] and de Ron [4]. Schnieders [5] presented also a validation with evacuated tubes solar collector. Himler et al. [6] presented a wide overview of partial differential equations calculation methods and validation with unglazed collector used for heating public outdoor swimming pool. One of the most advanced distributed-character models,

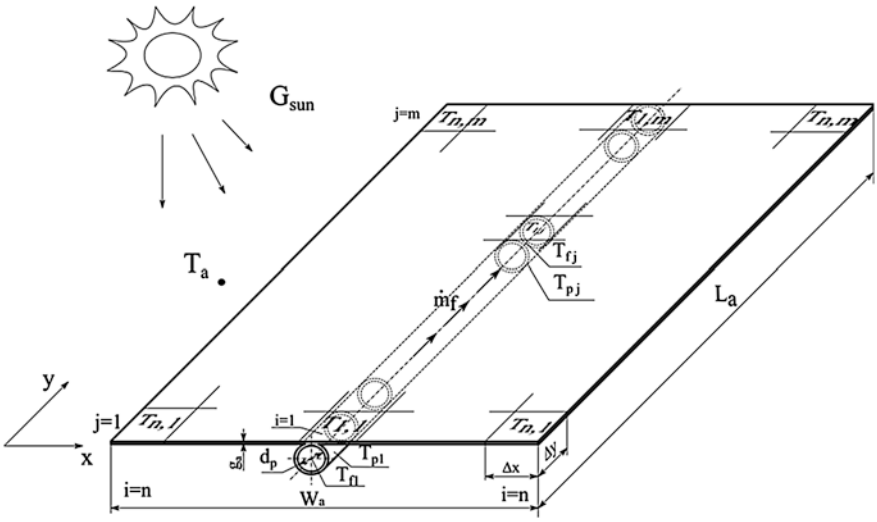

Fig. 3 The absorber fin discretization sketch

which can be used to obtain spatial temperature distribution inside the collector, was presented by Oliva et al. [7].

The model prepared to use in this paper assumes equal mass flow rate in each flow channel of solar absorber so there is only one fin section of absorber taken into consideration. Figure 3 shows the absorber fin divided into control volumes. For each collector component, in this case absorber plate, flow channel and working fluid, energy balance equations were derived.

The energy balance equation of heat fluxes in control volume of the absorber plate is formulated in cross-section of the absorber fin (Fig. 4).

Energy balance equation for the absorber plate is formulated as

$$q_{\text{acc}} = \Delta q_x - q_{\text{loss}} + q_a \tag{1}$$

where q_{acc}, Δq_x, q_{loss}, and q_a are energy fluxes of accumulation, conduction, heat loses, and absorbed solar radiation, respectively.

The absorber taken into consideration is the assembly of a flat-plate sheet metal with pipes welded into the uninsulated side of plate. The expanded form of absorber plate energy equation is written as follows [1]:

$$\begin{aligned}\rho_a c_a V_a \frac{\mathrm{d}T_a}{\mathrm{d}\tau} = &\left(-\lambda_a g_a \frac{\mathrm{d}T_a}{\mathrm{d}x}\right)\Big|_x - \left(-\lambda_a g_a \frac{\mathrm{d}T_a}{\mathrm{d}x}\right)\Big|_{x+\Delta x} \\ &- \left[\alpha_{\text{amb}}(T_a - T_{\text{amb}}) + \sigma\varepsilon_a\left(\frac{T_a}{100}\right)^4 - G_{\text{sun}}(\tau\alpha)\right]\Delta x\end{aligned} \tag{2}$$

where α_{amb} is the heat loss coefficient determined experimentally.

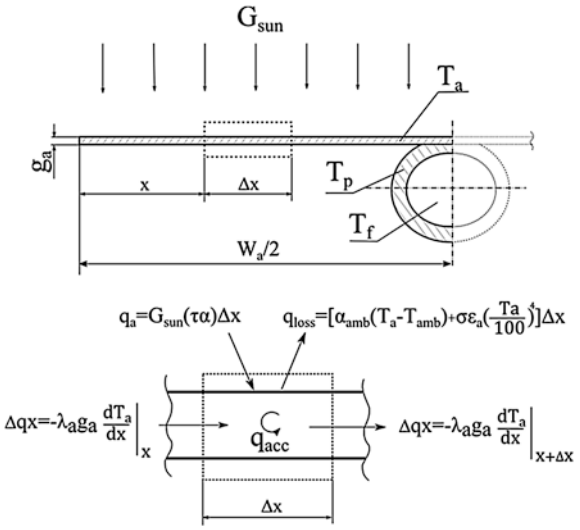

Fig. 4 Energy balance of absorber plate

In Eq. (2), spatial derivatives dT_a/dx are replaced by forward differential quotients

$$\left.\frac{dT_a}{dx}\right|_{i=0} = \frac{T_i - T_{i+1}}{\Delta x}; \left.\frac{dT_a}{dx}\right|_{x=W_a/2} = \frac{T_i - T_p}{\Delta x}$$

Thermal energy generated in the absorber plate is conducted into fluid channels through the homogeneous bonds. Figure 5 shows fluid channel energy balance.

The energy balance equation for the fluid pipe is formulated as

$$q_{\text{acc}} = \Delta q_y - q_{\text{loss}} + q_{a-p} \tag{3}$$

where q_{acc}, Δq_y, q_{loss}, and q_{a-p} are heat fluxes of accumulation in the flow channel, conduction in the flow channel, heat losses to ambient, and conduction between the absorber plate and the flow channel, respectively. The final form of flow channel energy balance is written as follows:

$$\begin{aligned}\rho_p c_p V_p \frac{dT_p}{d\tau} = &\left(-\lambda_a \pi S_p \frac{dT_p}{dy}\right)\Big|_y - \left(-\lambda_a \pi S_p \frac{dT_p}{dy}\right)\Big|_{y+\Delta y} \\ &- \left[\alpha_{\text{amb}} \pi D_p \left(T_p - T_{\text{amb}}\right) + \lambda_a g_a (T_p - T_a)\right]\Delta y\end{aligned} \tag{4}$$

Working fluid is heated by the walls of flow channels. In practice parts channels near to the absorber plate are hotter than bottom parts. This model assumes uniform temperature distribution in the cross section of the flow channel, equal to the temperature of the bond (Fig. 6).

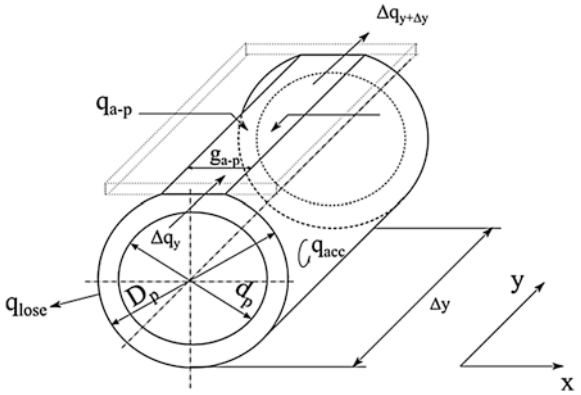

Fig. 5 The energy balance of fluid channel

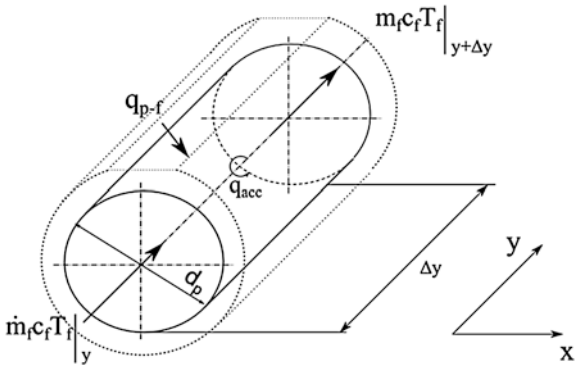

Fig. 6 Energy balance of working fluid

The energy balance for working fluid was formulated as

$$\rho_f c_f V_f \frac{\mathrm{d}T_f}{\mathrm{d}\tau} = \left(m_f c_f T_f\right)\big|_y - \left(m_f c_f T_f\right)\big|_{y+\Delta y} + \alpha_{p-f}\pi d_p (T_p - T_f)\Delta y \tag{5}$$

where α_{p-f} is the heat transfer coefficient on the boundary between pipes and working fluid, determined on the basis of Nusselt number, given by Heaton [1]:

$$\alpha_{p-f} = \frac{Nu_f \lambda_f}{d_p} \tag{6}$$

where:

$$Nu_f = 4.4 + \frac{0.00172\left(Re\,Pr\,\frac{d_p}{L}\right)^{1.66}}{1 + 0.00281\left(Re\,Pr\,\frac{d_p}{L}\right)^{1.29}}. \tag{7}$$

2.2 CFD Model

The second approach of solar collector simulation methods, often used to determine the efficiency of solar collectors, are CFD models built with CFD simulation software. Fan et al. [8] presented CFD solar collector model verified with experimental outdoor data. In this paper, the solar collector is modeled with assumption of uniform energy generation in the absorber tube and considering only a convective heat loss coefficient, calculated using external software *SolEffs* and set as an input for the CFD calculations. The comparison between calculated results and experimental data shows good agreement, especially in high flow rates. Furthermore, the authors show nonuniformity of the mass flow rate in absorber flow channels and discuss the influence of flow nonuniformity on the collector performance. Selmi et al. [9] presents 3D simulation of a flat-plate solar collector using the commercial CFD software *CFD-ACE*. The numerical results compared with experimental data, show good agreement in the analysed temperature profiles. Turgut and Onur [2] perform a numerical CFD analysis to determine the average heat transfer coefficients for forced convection air flow over a flat-plate solar collector surface.

To compare this method with the previously shown distributed-character modeling method, a simplified CFD model was built using code Fluent 12. The calculation domain of the proposed CFD solar collector model consist of the same physical components representation as previously: an absorber plate, fluid channels, and working fluid. However, in this case, all geometrical details of the absorber were taken into consideration. Figure 7 shows the geometric details of the calculation domain. Collector chasing is represented by convective and radiative heat loss from the absorber to ambient. The heat loss coefficient is estimated during thermal experiments of average absorber surface temperature and ambient collector temperature (Table 1).

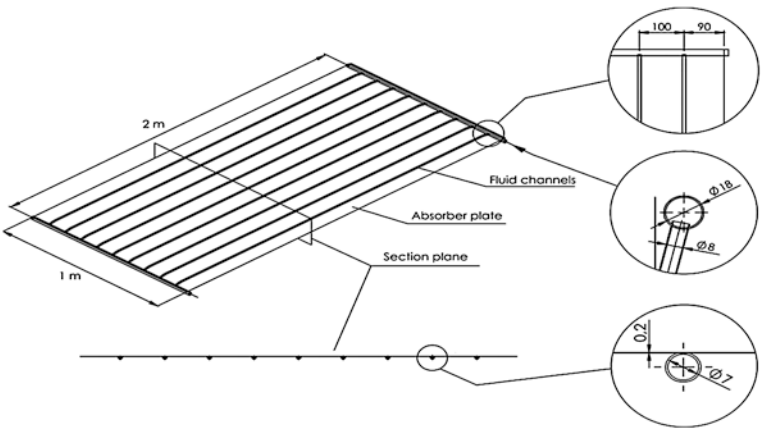

Fig. 7 CFD solar collector geometric model

Table 1 Solar collector KSH-2.0 technical specification

Technical parameters	KSH-2.0
Manufacturer/brand	KOSPEL inc./KSH-2.0
Collector type/gross area	Flat-plate/2 (m^2)
Absorber type	Parallel tube (harp)
Absorber material: plate/tubes	Copper/copper
Absorber connection method	Ultrasonic welding
Number of working channels	9
Number of manifolds	2
Working channels inner/outer diameter	$\phi 8/\phi 7$ (mm)
Manifolds inner/outer diameter	$\phi 18/\phi 16$ (mm)
Absorber coating/selectivity index	Blue Tec eta plus/19
Cover glass number/thickness	1/3.2 (mm)
Thermal insulation: bottom/sides	45/20 (mm)

Using the geometrical absorber model, the unstructured mesh was generated with the *ICEM-CFD* mesh tool. The absorber plate was meshed with hexahedron type of volume elements and all fluid channels and fluid domain were meshed with tetrahedral type cells.

Solar energy absorbed by an absorber was determined as

$$q_a = G_{\text{sun}}(\tau\alpha) \tag{8}$$

where G_{sun} is the solar irradiance (W/m^2) and $(\tau\alpha)$ is effective transmittance–absorption product (Fig. 8).

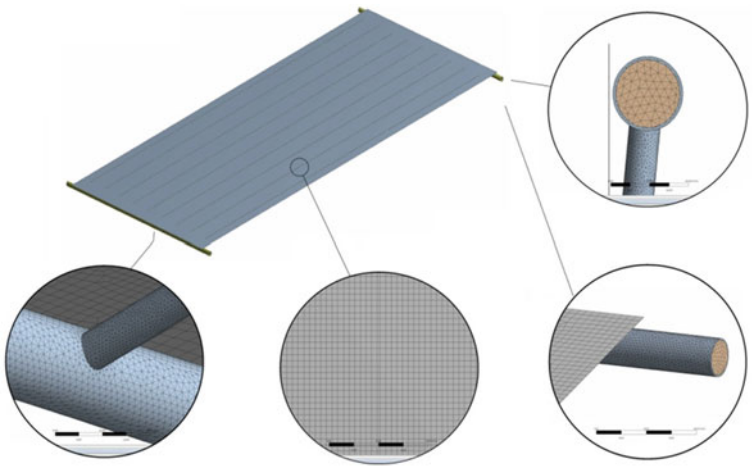

Fig. 8 Mesh setup of solar absorber model

In default operation conditions, a solar collector works in laminar flow conditions, so that a laminar flow model was used. In this case, *Fluent* will solve the governing conservation equations of mass, momentum, and energy. The governing equations are represented by a conservation equation for transport of a scalar quantity ϕ, written in an integral form for an arbitrary control volume V as follows [8]:

$$\oint_A \rho\phi v \cdot \mathrm{d}A = \oint_A \Gamma_\phi \nabla\phi \cdot \mathrm{d}A + \int_V S_\phi \mathrm{d}V \tag{9}$$

where $\oint \rho\phi \overrightarrow{v} \cdot \mathrm{d}\overrightarrow{A}$, $\oint \Gamma_\phi \nabla\phi \cdot \mathrm{d}\overrightarrow{A}$, $\int_V S_\phi \mathrm{d}V$ stand for change of parameter ϕ by convection, diffusion, and generation, respectively.

In the presented numerical approach, the natural-convection flow was taken into account by setting the fluid density ρ as a function of temperature, using the Boussinesq approximation

Fig. 9 Outdoor solar collector experimental setup

$$\rho = \rho_0(1 - \beta\Delta T) \tag{10}$$

where β is the fluid thermal expansion coefficient and ρ_0 is constant density of the flow (Fig. 9).

Calculation was performed in transient mode with pressure staggering option PRESTO and second-order upwind method for discretization of the momentum equations. The semi-implicit method (SIMPLE) was used to treat the pressure-velocity coupling. Calculation was considered converged when the scaled residuals for continuity equation, momentum equations, and energy equations fall below 1.0×10^{-4}, 1.0×10^{-4}, and 1.0×10^{-7}, respectively.

3 Experimental Work

Thermal measurements have been carried out with a 2 m^2 parallel tube flat-plate solar from KOSPEL Inc., Poland. Technical specification of tested collector is given in Table 2. Collector was tested in steady-state and transient conditions with artificial and natural solar radiation. Working fluid water was used. The inlet and outlet water temperature and ambient temperature was measured with RTD platinum sensors (Pt 100). The circulation of working fluid was forced by pump and the mass flow rate was measured using ENCO MPP-6 flow meter. Solar irradiance at collector front plane was measured with LP PYRA 02 pyranometer. The absorber surface temperature was measured during indoor test with thermocouple type "K". The position of measuring points is schematically shown in Fig. 10.

The data collection from RTD sensors, pyranometer, flow meter, ambient temperature sensor, and surface temperature sensor was executed by NI CompactDAQ data acquisition system and LabVIEW-2012 software. The accuracy of the measuring equipment is given in Table 3.

During the outdoor measurements, the incidence angle of solar radiation on collector surface was maintained manually in the range of $0° \leq \Theta\beta \leq 5°$, using solar pointer shadow. This angle correction rate was tested experimentally and the result shows a negligible effect on the thermal efficiency of the solar collector.

The absorber surface temperature, during an indoor test, was measured with artificial solar radiation. To simulate the solar radiation, a system of 28 metal-halide radiation sources was used. Radiation sources were embedded inside the aluminum luminaries on the tilting panel. To obtain uniform distribution of the radiation intensity at the collector mounting surface, several attempts have been carried out (Fig. 11). Each time, the power of radiation and distance between collector surface

Table 2 CFD model mesh parameters

Model component	Element type	Number of elements
Absorber plate	Hex	5.12×10^5
Flow channels	Tetra	3.73×10^6
Working fluid	Tetra	6.76×10^6

Fig. 10 Solar simulator radiation distribution measurement

Table 3 Accuracy of measuring equipment

Measured value	Measuring device	Accuracy
Inlet and outlet working fluid temperature	RTD—Pt 100	±0.1 K
Total solar irradiation	LP PYRA-02	±2 %
Mass flow rate	ENCO MPP-6	±1 %
Surface absorber temperature	Thermocouple type K	±0.5 K
Ambient temperature	RTD—Pt 100	±0.5 K

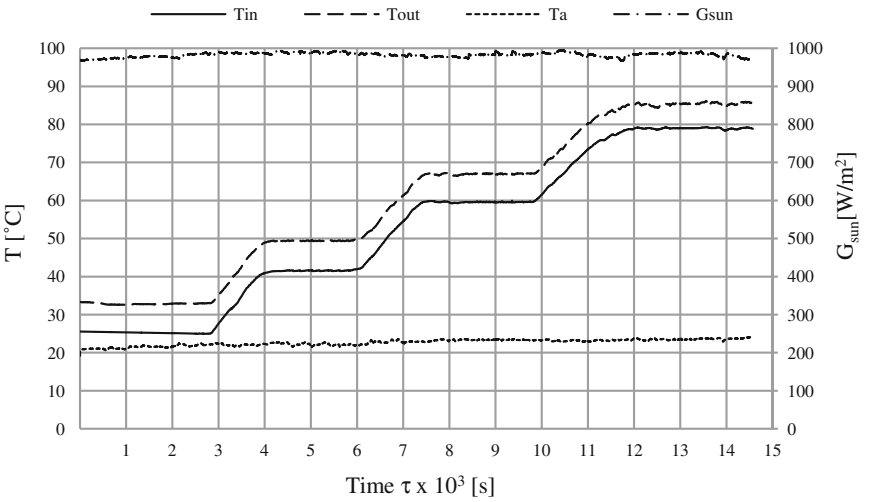

Fig. 11 Steady-state indoor measurement time graph

and solar simulator ware modified and measured in 80 points. The collimation procedure was stopped when the difference between extreme values and average value of radiation flux was smaller than 5 %.

4 Results and Discussion

To compare the results of numerical simulations and experiments, several measurements have been carried out. Firstly, the thermal efficiency characteristic $\eta(T \cdot m)$ was determined in a steady-state indoor test. According to EN ISO 9806:2013 standard, the second-order efficiency curve was statistically fitted to the values of collector efficiency measured for four different reduced temperature values $T \cdot m$. Each test point represents the average value of thermal efficiency from 30 min measurement period, with constant radiation and inlet fluid temperature value.

The actual useful power $\dot{Q}_u$, for each test point, was calculated from

$$\dot{Q}_u = \dot{m} \cdot c_f \cdot \Delta T_f \tag{11}$$

where $\dot{m}$ was obtained from volumetric flow rate measurement with density determined for the temperature of fluid in flow meter.

Thermal efficiency η for each test point was calculated from

$$\eta_i = \frac{\dot{Q}_u}{A_a \cdot G_{\text{sun}}} \tag{12}$$

Test data were correlated by curve fitting using least square method to obtain the thermal efficiency function of the form (Table 4)

$$\eta = \eta_0 - a_1(T \cdot m) - a_2 G_{\text{sun}}(T \cdot m)^2 \tag{13}$$

After the experiment, the numerical calculation was performed. Each step of steady-state measurement points was treaded separately. Boundary conditions for each steady-state point were represented by average values of mass flow rate, inlet fluid temperature, ambient temperature, and solar radiation flux which recorded

Table 4 Steady-state outdoor experiment data

T_{in} (°C)	T_{out} (°C)	T_{a} (°C)	G_{sun} (W/m^2)	ṁ (kg/h)	$T \cdot m$ (m^{2}K/W)	η_{i}
25.1	32.8	21.8	980	139.9	0.00	0.74
41.5	49.4	22.1	990	140.0	0.02	0.68
59.6	67.0	23.4	984	139.5	0.04	0.62
79.0	85.6	23.6	987	140.0	0.06	0.53

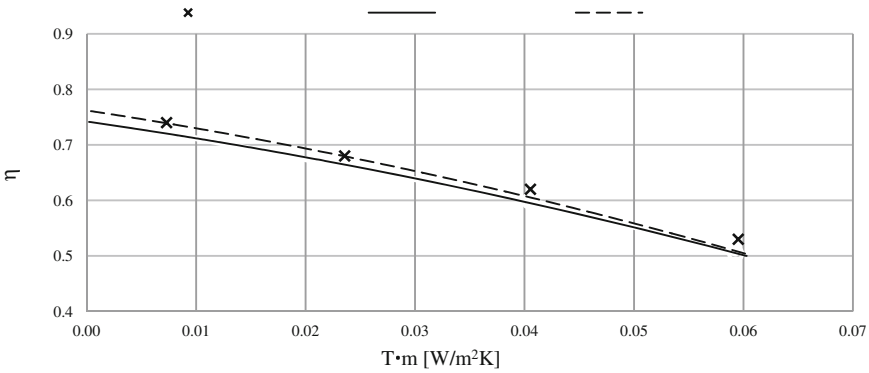

Fig. 12 The results of steady-state thermal efficiency measurement and numerical calculations

Table 5 Second-order efficiency curve η coefficients

Based on absorber area	η_o	a_1 (W/m^2 K)	a_2 (W/m^2 K)
η—experiment	0.76	2.9	0.017
η—D-C model	0.74	2.8	0.02
η—CDF model	0.76	3.0	0.021

during corresponding measurements. The results of numerical calculations between D-C and CFD models compared with the experiments are shown in Fig. 12.

As shown in Fig. 12, the results of numerical calculations using D-C and CFD models are in good agreement with the experiment. In case of CFD model result, the correlation with the experiment around the low values of $T \cdot m$ is almost perfect (Table 5).

The values of optical efficiency η_0, determined by experiment and CFD calculations, are the same with accuracy of two decimals. With increasing $T \cdot m$ value, the convergence of *CFD* model results and experiments decreases. The reason of divergence in results within high values of $T \cdot m$ can be caused by underestimation of heat loss coefficient.

In case of D-C model, the calculated efficiency curve goes below all measured values in similar distance from each measured points. This can be caused by simplification of absorber construction characteristics, contained in the model.

To investigate the relationship between the absorber design and the heat exchange process, the absorber surface temperature was measured experimentally and calculated with D-C and CFD models. The absorber surface temperature was measured through the back side of collector housing. During the surface temperature measurements, the inlet fluid temperature was set to meet the least heat loss conditions

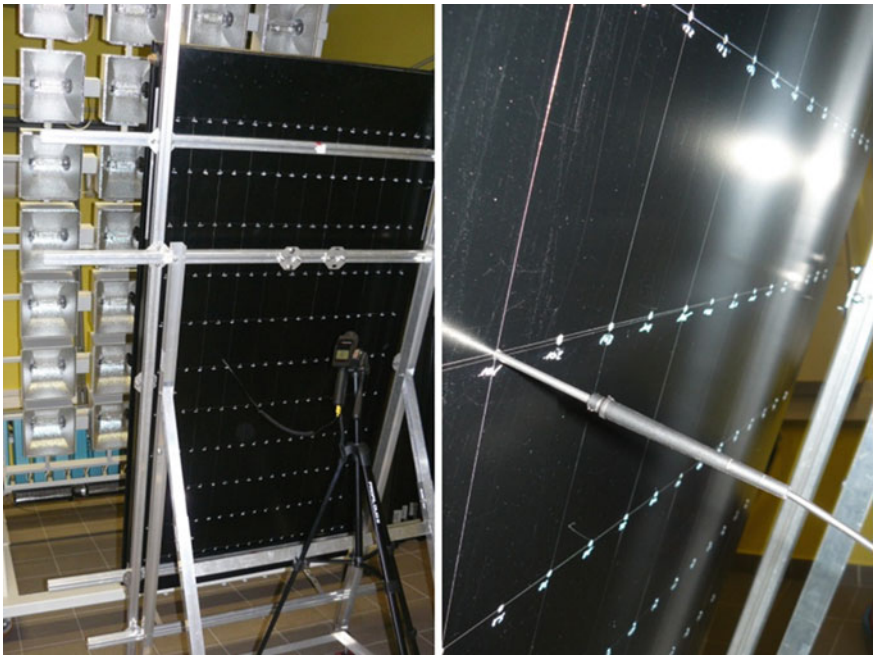

Fig. 13 Absorber temperature measurements

$$T_{\text{in}} + \Delta T/2 \cong T_a \tag{14}$$

The absorber surface temperature was measured in four different profiles. Each profile consisted of 19 temperature points, measured one by one. The profiles and measure point distribution are shown in Figs. 10 and 13.

All measured temperature values in each profile were imposed on numerically determined absorber temperature surface calculated with D-C model. As shown in Fig. 15 middle section of the absorber has temperature comparable to calculated values in this region. The agreement of the result is especially high for the absorber plate, measured between flow pipes, whereas flow pipe wall temperature seems to be higher than calculated results. Higher fluid wall channel temperature can be caused by not exactly laminar flow regime and higher heat transfer coefficient in near wall fluid zones. Those differences can be reduced by tuning the model parameters. The most important is that the agreement of numerical and experimental results is much lower for the edge zones of the absorber. The absorber temperature measured in edge zones is often more than 20 % higher than the calculated values (Fig. 14).

The reason for results disagreement, in the side edge zones of absorber, lies in different geometry of marginal fins. In this particular solar collector, the edge fins of absorber are larger than the middle ones. This means that the first and last fluid pipe cooperates with a larger absorption surface, than the others. This geometric feature

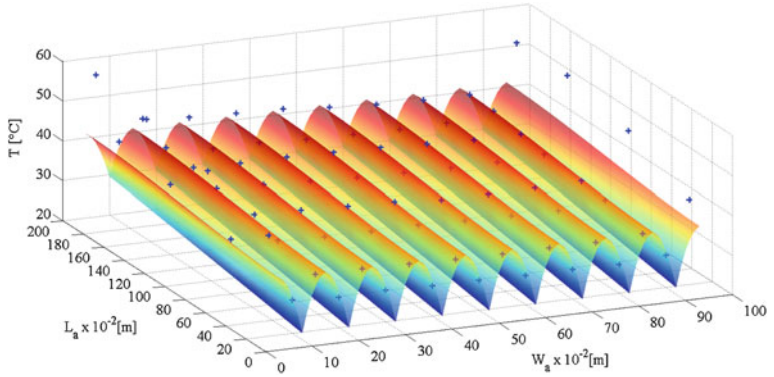

Fig. 14 Absorber surface temperature calculated using D-C model, with experimentally measured temperature points

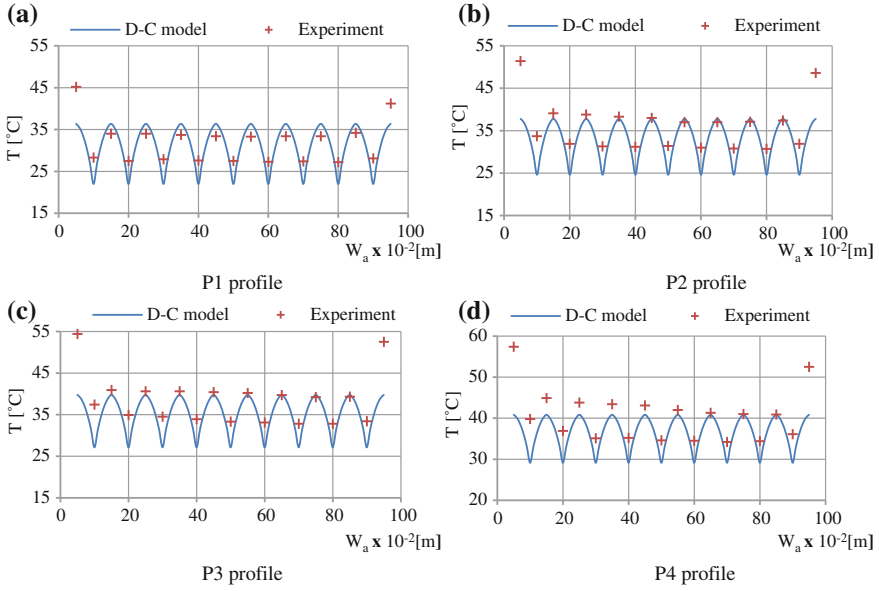

Fig. 15 The result of absorber temperature investigation with experimental measurements and D-C model simulation

of this particular solar absorber is shown in Fig. 7. As a result, the conduction of heat flux from the edge zone of the absorber plate has a longer distance to cover, which causes heat energy damming in edge regions of the absorber.

This effect can be clearly seen in Fig. 15, where measured temperature points and calculated temperature values are presented in each profile.

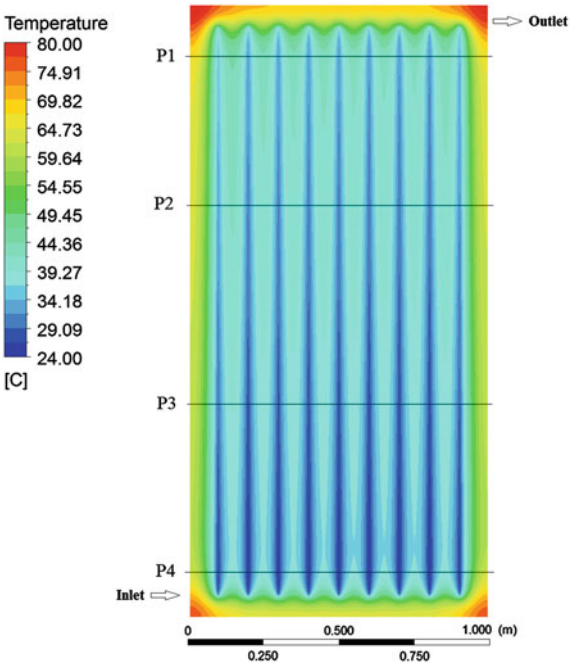

Fig. 16 The result of absorber surface temperature distribution from *CFD* model with experimentally examined cross sections marked

For the same collector working conditions, the *CFD* analysis was carried out. As it was mentioned before, all geometrical details of the absorber were considered and fluid local density was approximated. The results of the absorber temperature values, obtained from CFD model, were compared with the previously collected experimental data. In Fig. 16, the result of the absorber surface temperature distribution is shown.

The *CFD* simulation result shows the consequences of geometric irregularity of marginal absorber fins. Observed experimental high-temperature values on the edge of the absorber, has been mapped with good agreement with experiment. The comparison of measured temperature points values and *CFD* calculated temperature values, in each profile, are presented in Fig. 17.

The *CFD* analysis has proved a strong dependency between the geometrical details of absorber design and heat exchanging process. Measurement data is in better agreement in comparison with D-C modeling method.

Both methods were also compared to experimental data from long-term outdoor test. This investigation was performed to verify which method is more suitable for long-term efficiency calculations. In order to examine both approaches for transient states, strongly dynamic conditions of experimental data were selected (Fig. 17).

The result of experimentally measured useful power $\dot{Q}_u$, extracted from collector and numerical results from D-C and *CFD* models are shown in Fig. 18.

Based on numerical and experimental results, the root mean square values of useful energy $\dot{Q}_{u\mathrm{RMS}}$, extracted from solar panel were determined as follows:

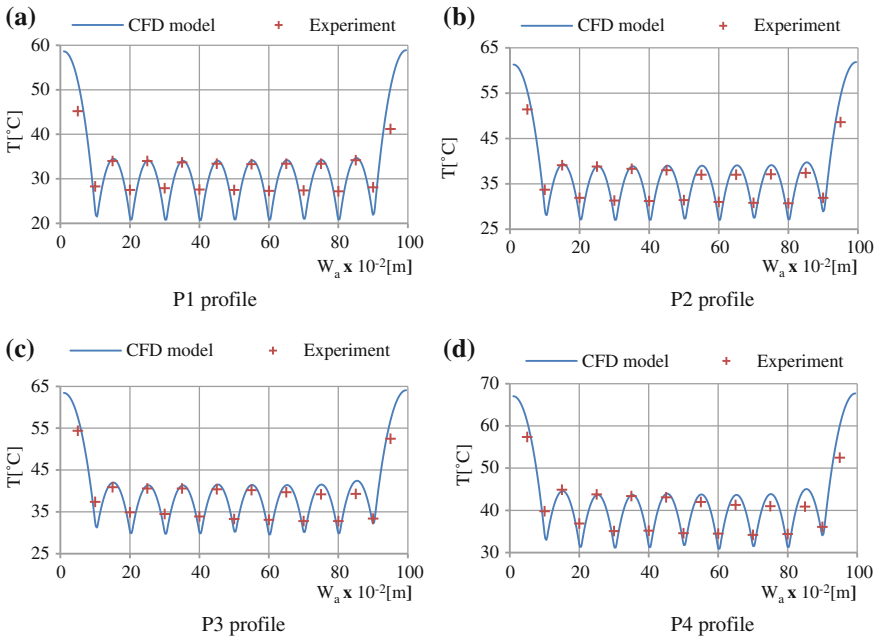

Fig. 17 The result of absorber temperature investigation with experimental measurements and CFD model simulation

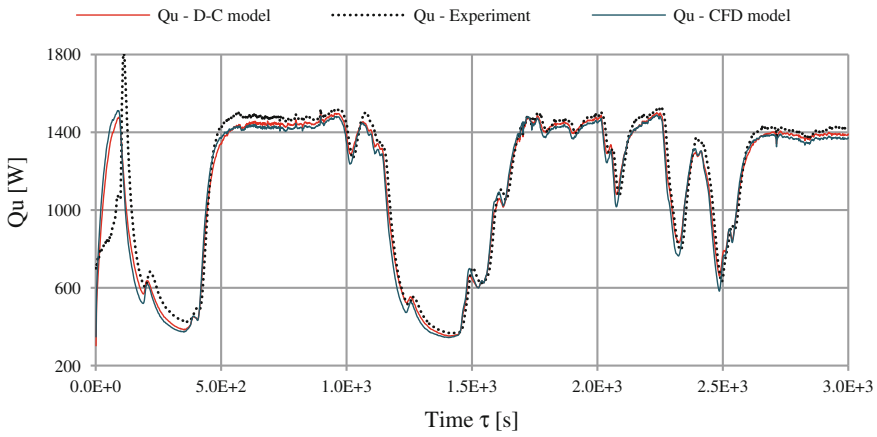

Fig. 18 Measured experimentally and calculated useful energy Q_u extracted from solar collector during outdoor test, with mass flow rate $\dot{m}_c = 140\,\mathrm{kg/h}$

Table 6 RMS values of experimental and calculated useful energy $\dot{Q}_u$

	Experiment	*D-C* model	*CFD* model
$\dot{Q}_{u_{\mathrm{RMS}}}$ (W)	1212.3	1191.3	1181.7

Table 7 Correlation coefficients for D-C and CFD model results in relation to the experiment

	D-C model	*CFD* model
R_{e-s}	0.968	0.951

$$\dot{Q}_{u_{\mathrm{RMS}}} = \sqrt{\frac{1}{n}\sum_{i=1}^{n}(\dot{Q}_{u_i})^2} \tag{15}$$

where i—is the measuring sample (Table 6).

In order to quantify the convergence of experimental and simulation results, the multidimensional correlation coefficients R_{e-s} were determined as follows (Table 7):

$$R_{e-s} = \sqrt{1 - \frac{\sum_{i=1}^{n}(Q_{u_i} - Q_{u_{Ex}})^2}{\sum_{i=1}^{n}(Q_{u_{Ex}} - Q_{u_{AV}})^2}} \tag{16}$$

The results of useful energy Q_u obtained using proposed simulation methods are satisfactorily accurate. In both cases, the value of calculated RMS energy gain differs from the experiment of less than 3 %. The correlation coefficient R sums to confirm a good result agreement. In light of this analysis, proposed numerical simulation methods can be used to estimate the energy yield from flat-plate solar collector in variable insolation conditions, with high accuracy.

5 Conclusion

Two different numerical simulation methods of flat-plate solar collectors' heat exchanging process are presented in this paper. All calculated results were compared with experimental steady-state and transient data. The absorber surface temperature, obtained with tested numerical models, was verified by contact temperature measurements through the back side of collector housing.

The steady-state indoor investigation shows good agreement between calculated and measured results. Determined numerical solar collector efficiency curves $\eta(T \cdot m)$ were sufficiently similar to EN ISO 9806 standard test result, which means that the basic exploitation parameters, like optical efficiency η_0 and heat loss coefficients, can be found with high accuracy. The difference between these approaches is noticeable if time consumption is taken into evaluation. The D-C

simulation model can be formulated quite fast and the solution can be found using standard *PC* in short time, while *CFD* modeling method requires much larger computational effort. Therefore, in order to quantify the solar collector efficiency, low-cost distributed-character modeling method is suggested.

Because of wide simplifications of lumped capacitance, D-C solar collector models it is difficult to analyze the construction design and optimize its geometric and structural configurations. For this research area, *CFD* method seems to be essential. Presented in this work, *CFD* analyses of KSH-2.0 solar collector allowed to detect some design misstatements, identified by high temperature values in the edges of absorber plate. The local temperature of the absorber plate is the authoritative determinant of the local heat removal factor. Detected high temperature of marginal fins will cause greater heat loss to the ambient, and consequently, marginal fins will have lower thermal efficiency. Higher temperature of fluid in marginal fins will also cause greater inequality of mass flow rate in other pipes, which contributes to the reduction of solar collector performance. Similar analysis could not be done with distributed-character model without an edge correction factor.

Long-term investigations, with various environmental conditions show good agreement of experimental and calculated results. However, to optimize the energy yield during operations in any working conditions, in order to optimize the regulation criteria for control systems, fast modeling method is needed. Universal *CFD* modeling method can be used, in many applications, were result resolution and accuracy are more important than calculation time. The optimization process which often involves looped model start-up, D-C modeling method is suggested.

References

1. Duffie, J.A., Beckman, W.A.: Solar engineering of thermal processes, 3rd edn. Wiley Interscience, New York (2006)
2. Turgut, O., Onur, N.: Three dimensional numerical and experimental study of forced convection heat transfer on solar collector surface. Int. Commun. Heat Mass Transfer **36**(3), 274–279 (2009)
3. Kamminga, W.: The approximate temperatures within a flat-plate solar collector under transient conditions. Int. J. Heat Mass Transf. **28**(8), 433–440 (1985)
4. de Ron, A.J.: Dynamic modeling and verification of a flat-plate solar collector. Sol. Energy **24** (2), 117–128 (1980)
5. Schnieders, J.: Comparison of the energy yield predictions of stationary and dynamic solar collector models and the model's accuracy in the description of a vacuum tube collector. Sol. Energy **61**, 179–190 (1997)
6. Hilmer, F.,Vajen, K., RatkaA., Ackermann, H., Fuhs, W., Melsheimer, O.: Numerical solution and validation of dynamic model of solar collectors working with varying flow rate. Sol. Energy **65**(5), 305–321 (1999)
7. Oliva, A., Costa, M., Perez Segarra, C.D.: Numerical simulation of solar collectors: the effect of nonuniform and nonsteady state of the boundary conditions. Solar Energy **47**(5), 359–373 (1991)

8. Fan, J., Shah, L., Furbo, S.: Flow distribution in a solar collector panel with horizontally inclined absorber strips. Sol. Energy **81**(12), 1501–1511 (2007)
9. Selmi, M., Al-Khawaja, M., Marafia, A.: Validation of CFD simulation for flat plate solar energy collector. Renew. Energy **33**, 383–387 (2008)